INTERNATIONAL JOURNAL FOR NUMERICAL METHODS IN FLUIDS
Int. J. Numer. Meth. Fluids 2007; **55**:723–735
Published online 17 April 2007 in Wiley InterScience (www.interscience.wiley.com). DOI: 10.1002/fld.1483

Instabilities during batch sedimentation in geometries containing obstacles: A numerical and experimental study‡

Rekha R. Rao[1,*,†], Lisa A. Mondy[1] and Stephen A. Altobelli[2]

[1]*Sandia National Laboratories, Albuquerque, NM 87185, U.S.A.*
[2]*New Mexico Resonance, Suite C1, Yale Center, Albuquerque, NM 87108, U.S.A.*

SUMMARY

Batch sedimentation of non-colloidal particle suspensions is studied with nuclear magnetic resonance flow visualization and continuum-level numerical modelling of particle migration. The experimental method gives particle volume fraction as a function of time and position, which then provides validation data for the numerical model. A finite element method is used to discretize the equations of motion, including an evolution equation for the particle volume fraction and a generalized Newtonian viscosity dependent on local particle concentration. The diffusive-flux equation is based on the Phillips model (*Phys. Fluids A* 1992; **4**:30–40) and includes sedimentation terms described by Zhang and Acrivos (*Int. J. Multiphase Flow* 1994; **20**:579–591). The model and experiments are utilized in three distinct geometries with particles that are heavier and lighter than the suspending fluid, depending on the experiment: (1) sedimentation in a cylinder with a contraction; (2) particle flotation in a horizontal cylinder with a horizontal rod; and (3) flotation around a rectangular inclusion. Secondary flows appear in both the experiments and the simulations when a region of higher density fluid is above a lower density fluid. The secondary flows result in particle inhomogeneities, Rayleigh–Taylor-like instabilities, and remixing, though the effect in the simulations is more pronounced than in the experiments. Published in 2007 by John Wiley & Sons, Ltd.

Received 20 October 2005; Revised 6 February 2007; Accepted 11 February 2007

KEY WORDS: suspensions; instabilities; sedimentation

1. INTRODUCTION

Suspensions of non-neutrally buoyant particles are found in a variety of industries from food processing to microelectronics to chemical and petroleum. The particles will settle or float

*Correspondence to: Rekha R. Rao, Sandia National Laboratories, MS 0836, Albuquerque, NM 87185-0836, U.S.A.
†E-mail: rrrao@sandia.gov

Contract/grant sponsor: D.O.E. Office of Science Advanced Computing Research (ASCR)

depending on whether they are lighter or heavier than the suspending fluid. In this paper, we are interested in the sedimentation or flotation of particles in complex geometries with obstructions. For quiescent settling experiments in simple geometries, the behaviour of the particles is monotonic and generally follows the 1-D theory of Kynch [1]. Once settling begins, three distinct layers form: one of pure suspending fluid; one of suspension at the average concentration; and one of sediment at or near the maximum packing. (The sediment layer can show some consolidation over time, which can increase the particle concentration.) These three layers are all characterized by a flat sharp interface, or volume fraction shock, for mono-modal particle distributions. For more polydisperse systems, the suspension tends to size segregate creating multiple suspension layers with different particle radii [2].

Numerical studies of suspension flow using continuum methods have been investigated by a number of groups for suspensions of neutrally buoyant [3–7] and sedimenting particles [8–12]. These papers all use a single-phase description of the suspension and either a diffuse flux [13] or a suspension balance constitutive equation [14]. Numerical methods used range from finite volume to finite element and finite difference methods. The geometries previously investigated include Couette, expansion flows, and flow down inclined channel, but did not include both sharp flow feature and non-neutrally buoyant particles that can lead to instabilities.

Instabilities have been widely observed experimentally in suspension flow and are often seen in neutrally buoyant particles in free-surface flows. These instabilities can be associated with particle-scale phenomena such as fluid surface tension on the particle surfaces and normal forces. Tirumkudulu *et al.* [15] and Timberlake and Morris [16] saw axial banding instabilities in partially filled Couette devices in shear flow, whereas Timberlake and Morris [17] saw ribbing-type instabilities in suspension films on an inclined plane. Tang *et al.* [18] observed viscous fingering in a radial Hele–Shaw cell of a neutrally buoyant suspension displacing air. Linear stability theory has been used to understand rimming flows in partially filled Couettes with free surfaces for neutrally buoyant particles [19], flow down an inclined-plane for non-neutrally buoyant particles [20], and flow in an inclined settler [21]. Linear stability in a fluidized bed at the dilute limit has been investigated by Hernandez [22], who determined that instabilities occur as suspensions reach higher concentration due to flow. Spectral simulations from this work showed Rayleigh–Taylor-like instabilities at the unstable conditions predicted from the linear analysis. Similar instabilities have been observed in inclined batch settlers where vortices appear at the suspension–pure fluid interface. These instabilities have been analysed with analytical methods [2].

Here we use transient finite element simulations and nuclear magnetic resonance imaging to examine instabilities that form through a combination of gravity and geometry, with no external shear flow. Thus, the flow is purely driven by the sedimentation/flotation and the instabilities themselves. Since this is primarily an inertial phenomena, we believe it is well suited to being understood using a continuum approach. By inertial phenomena, we mean density driven since the Reynold number based on the Stoke velocity and particle diameter is small, much less than one, but the Grashof number, based on the density difference and the macroscopic length scale is in the forties. This in turn, yields a large Rayleigh number for buoyancy-driven flow, defined as the Grashof number divided by the Reynold number squared.

For the flows in the complex geometries described here, we get the primary flow from sedimentation, but have additional secondary flows that are driven by Rayleigh–Taylor instabilities created by regions of high-density fluid being above a low-density one. The instabilities lead to vortices, remixing and viscous resuspension of the suspension [23] causing a more diffuse and irregular interface between the suspension and the pure fluid, even for mono-modal suspensions.

Published in 2007 by John Wiley & Sons, Ltd. *Int. J. Numer. Meth. Fluids* 2007; **55**:723–735
DOI: 10.1002/fld

The first section of this paper details our experimental method using nuclear magnetic resonance imaging (NMR) to determine the particle volume fractions as they evolve over time. In the following section, we give a brief recap of the theory and numerical method, which can be found elsewhere [12]. The problems investigated include sedimentation in a cylinder with a contraction, particle flotation in a horizontal cylinder with a horizontal rod, and flotation around a rectangular inclusion. Section 4 documents experimental details such as fluid and particle properties for the three experiments of interest. We investigate particles that are heavier and lighter than the suspending fluid depending on the experiment. The results from the experiments are presented and compared to the numerical results. Finally, we conclude the paper with discussion and directions for future work.

2. EXPERIMENTAL METHOD

Previous NMR studies have demonstrated that imaging may be used to study hindered settling, and also to study interfacial broadening [24, 25]. Previously, we used NMR measurements of the liquid fraction as a function of the vertical coordinate y and time t to measure the hindered settling function for a range of concentration in a single-batch experiment [26]. These studies all involved 1-D imaging and flow geometries with constant cross-sectional area. The experiments described here used 2-D imaging to visualize particle motion in more complex systems in a similar manner to Rao *et al.* [12]

The NMR imaging experiments were performed in a 1.89 T horizontal-bore, super-conducting magnet equipped with shielded gradient coils (Magnex, Inc., Boston, MA) and controlled by a Tecmag (Houston, TX) Libra. The r.f. probe was a custom-built high-pass birdcage [27]. Spin echo, spin warp imaging [28] was performed with an echo time of 4 ms and repetition times of 50–100 ms. Since these repetition times are shorter than T1, low-angle pulses were used for excitation and spoiling gradients were applied during the recycle time. Single vertical slices were collected on resonance, and the imaging gradients were all less than 2 G/cm. Details of the method can be found in Callaghan [28].

3. NUMERICAL MODEL

3.1. Equations

As discussed in Rao *et al.* [12], a model based on Phillips *et al.* [13] and Zhang and Acrivos [8] was used to understand how the particle concentration evolves for problems with non-neutrally buoyant particles in both quiescent settling and flotation. Since the particles have a different density than the suspending fluid, the density depends on the local particle concentration. If ρ_f and ρ_s are the mass concentrations of the fluid phase and particle phase, respectively, then, the total density becomes

$$\rho = \rho_f + \rho_s = (1 + \phi)\rho_f^0 + \phi\rho_s^0 = \rho_f^0 + \phi(\rho_s^0 - \rho_f^0) = \rho_f^0 + \phi\Delta\rho \tag{1}$$

where ϕ is the particle-phase volume fraction, ρ_f^0 and ρ_s^0 are the pure phase densities, and $\Delta\rho$ is the difference between the solid particle density and the pure fluid density. The variable density leads to a buoyancy-driven flow source term in the momentum equation. The momentum equation

has a generalized Newtonian viscosity, which depends on the local particle concentration *via* the Krieger model [29]:

$$\rho\frac{\partial v}{\partial t} + \rho\mathbf{v}\cdot\nabla\mathbf{v} + \nabla p - \nabla\cdot(\mu(\nabla v + \nabla v^t)) + \Delta\rho\phi\mathbf{g} = 0 \tag{2}$$

$$\mu = \mu_0\left(1 - \frac{\phi}{\phi_\mathrm{m}}\right)^{-n} \tag{3}$$

where $\mathbf{v}$ is the suspension velocity, p is the dynamic pressure, $\mathbf{g}$ is the gravitational acceleration, and t is the time, μ_0 is the suspending fluid viscosity, n is a parameter that is used to best fit the viscosity data (1.82 is used in this work), and ϕ_m is the particle concentration at maximum packing.

Since the density is variable, the full continuity equation must be used:

$$\frac{\partial\rho}{\partial t} = -\nabla\cdot\rho v \tag{4}$$

If we substitute in Equation (1) for the definition of density in terms of particle volume fraction and the two pure phase densities, we get the divergence of velocity in terms of an evolution equation for particle volume fraction:

$$\rho_\mathrm{f}^0\nabla\cdot v = \Delta\rho\left(\frac{\partial\phi}{\partial t} + \nabla\cdot(v\phi)\right) \tag{5}$$

The parenthetical expression on the left-hand side of Equation (5) is defined as the particle flux:

$$\frac{\partial\phi}{\partial t} + \nabla\cdot(v\phi) = \frac{1}{\rho_\mathrm{s}^0}\nabla\cdot\mathbf{J}_\mathrm{s} \tag{6}$$

Substituting Equation (6) into Equation (5) yields a source term that arises in the continuity equation based on the variable density, related to the particle flux, $\mathbf{J}_\mathrm{s}$.

$$\nabla\cdot v = \frac{\Delta\rho}{\rho_\mathrm{s}^0\rho_\mathrm{f}^0}\nabla\cdot\mathbf{J}_\mathrm{s} \tag{7}$$

Though both the particle and suspending fluid are incompressible, the continuity equation is no longer solenoidal due to the fact that the density varies with local volume fraction.

The particle concentration is determined from substituting the incompressibility constraint, Equation (7), into the particle conservation equation (6) [see [12] for details]:

$$\frac{\partial\phi}{\partial t} + v\cdot\nabla\phi = -\left(\frac{\rho_\mathrm{f}^0 + \phi\Delta\rho}{\rho_\mathrm{s}^0\rho_\mathrm{f}^0}\right)\nabla\cdot\mathbf{J}_\mathrm{s} = \frac{\rho}{\rho_\mathrm{s}^0\rho_\mathrm{f}^0}\nabla\cdot\mathbf{J}_\mathrm{s} \tag{8}$$

The particle flux, $\mathbf{J}_\mathrm{s}$, has three terms involving variations of shear-rate invariant and concentration, viscosity and gravity:

$$\frac{\mathbf{J}_\mathrm{s}}{\rho_\mathrm{s}^0} = -(\phi D_\phi\nabla(\dot\gamma\phi) + \phi^2\dot\gamma D_\mu\nabla(\ln\,\mu)) + f v_\mathrm{s}\phi \tag{9}$$

$$D_\phi = 1.05\phi D_\mu, \quad D_\mu = 0.651a^2 \tag{10}$$

where the diffusion coefficients used are obtained from Tetlow *et al.* [30]. In addition, a small amount of numerical diffusion in a Fickian form must be added to stabilize the concentration fronts that occurs. Values of the numerical diffusivity are on the order of two orders of magnitude smaller than the diffusivities given in Equation (7).

The shear-rate tensor and its magnitude are defined in the standard way:

$$\dot{\gamma} = (\nabla v + (\nabla v)^t), \quad \dot{\gamma} = \sqrt{\tfrac{1}{2}(\dot{\underset{\sim}{\gamma}}, \dot{\underset{\sim}{\gamma}})} \tag{11}$$

The buoyancy terms in the flux comprised a Stokes velocity and a hindered settling function:

$$v_s = \frac{2}{9}\frac{a^2(\rho_f^0 - \rho_s^0)\mathbf{g}}{\mu_0}, \quad f = \frac{\mu_0(1-\phi^{av})}{\mu} \tag{12}$$

where average concentration, ϕ^{av}, is the initial concentration.

3.2. Numerical method

The momentum equation (2), the continuity equation (4), the particle conservation equation (5), and shear-rate invariant equation (8) are discretized with the Galerkin finite element method. The unknowns are velocity, pressure, particle volume fraction, and the scalar shear-rate invariant. Velocity unknowns are interpolated with biquadratic shape functions, while bilinear shape functions are used for all other variables. Rectangular Lagrangian elements are used. For the momentum equation, time integration is carried out using a second-order Crank–Nicholson finite difference discretization. For the concentration equation, because of the sharp fronts created during settling, a Taylor–Galerkin method is used [31].

We solve the nonlinear problem using a Newton–Raphson linearization scheme, which results in a matrix of unknowns that we solve simultaneously using direct or iterative solvers. Details of the finite element discretization and linearization scheme can be found in our previous paper [12].

4. RESULTS

4.1. Batch sedimentation in a cylinder with a contraction

4.1.1. Problem description. A quiescent settling experiment was carried out in a cylinder with a contraction roughly two-thirds of the way up to investigate the effect of a horizontal obstruction on particle settling. The geometry and dimensions can be seen in Figure 1. The suspension was made of PMMA particles in a suspending fluid composed of 22% water and 78% glycerol. The glycerol solution was formulated such that the PMMA particles had a slightly higher density than the suspending fluid, and would settle out relatively slowly. The suspension properties are presented in Table I.

4.1.2. Simulations and comparison with experiment. Axisymmetric finite element simulations were carried out for this geometry and material properties. The mesh and boundary conditions are given in Figure 1. The mesh contains 7073 nodes and 1720 elements, yielding 19 597 unknowns. We specify no slip at the solid boundary and symmetry about the centreline. The initial concentration distribution is homogeneously distributed at 19.2% by volume.

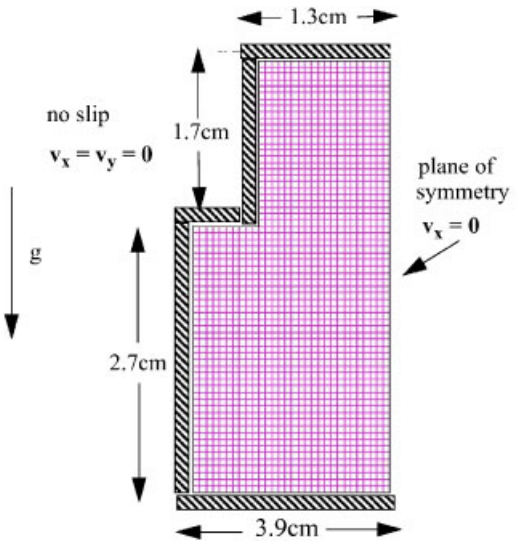

Figure 1. Finite element mesh and boundary conditions for particles settling in a cylinder with a contraction.

Table I. Density, viscosity, and particle data for cylinder experiment.

Quantity	Value
Density PMMA, ρ_s^0	1.18 g/cm^3
Density glycerol/water solution, ρ_f^0	1.1755 g/cm^3
Viscosity glycerol/water solution, μ_0	0.184 g/cm s
Maximum volume fraction, ϕ_{max}	0.64
Initial volume fraction, ϕ_0	0.192
Particle radius, a	0.0397 cm

Results from NMR imaging and finite element simulation are given in Figure 2. For the finite element simulations, we see clear fluid regions developing at the top of the cylinder and directly under the contraction. A zone of maximum packing forms at the bottom of the container as particles pile up. Over time, the clear layers under the contraction release a bubble of fluid that moves down the gravimetric potential towards the top of the cylinder. Once the blob of pure fluid reaches the suspension–pure fluid interface near the top of the container, its momentum begins to deform it, causing the interface to bulge upward. The layer of high-density suspension over a lower-density blob of pure fluid causes a Rayleigh–Taylor instability, which results in remixing and recirculation near the suspension–pure fluid interface. This causes pure fluid to move downward and suspension to move upward, counter to their natural inclination. Once the interface moves below the obstruction, the settling becomes monotonic. However, because of the instability, the final distribution of particles is slightly concave up instead of flat as it would be for settling in a cylinder without an obstruction.

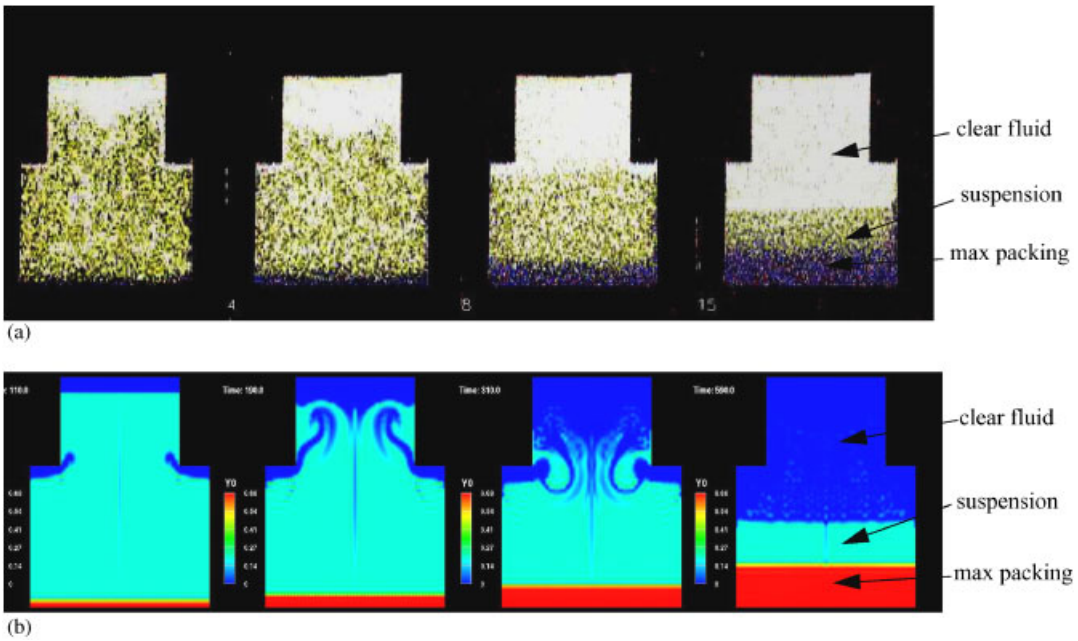

Figure 2. Particles settling in a cylinder with a contraction for a 0.192 volume fraction of 0.0397 cm radius PMMA particles in glycerol/water suspending fluid. Particles are slightly heavier than the fluid: (a) NMR imaging at times $t = 105$, 175, 315, and 560 s and (b) finite element simulations at $t = 110$, 190, 310, and 590 s.

The NMR imaging show results qualitatively similar to the modelling though the discrete particles do not give as much detail as the continuum modelling. Initially, we get clear zone forming underneath the horizontal surfaces and particles settling on the bottom of the container. Over time, we can see that the suspension–pure fluid interface become V-shaped near the centre of the cylinder and is not flat. The final distribution of particles is also concave up. Although still images cannot capture the movement, a video produced from the NMR images clearly shows recirculation occurring in the upper portion of the container.

4.2. Quiescent particle flotation in a horizontal wide gap Couette

4.2.1. Problem description. Batch flotation of PMMA particles in a 96% glycerol, 4% water solution, was carried out in a horizontal wide gap concentric Couette in order to investigate the effect of a circular obstruction on settling behaviour. Properties for the particles and suspending fluid are given in Table II. The particles are slightly less dense than the suspending fluid, causing them to float. The Couette geometry can be seen in Figure 3. The inner rod is one-fourth the size of the outer cylinder. Both are stationary throughout the experiment.

4.2.2. Simulation and comparison with experiment. The finite element mesh and boundary conditions are given in Figure 3. We specify no slip at the inner rod and the outer cylinder surfaces.

Table II. Density, viscosity, and particle data for Couette experiment.

Quantity	Value
Density PMMA, ρ_s^0	1.18 g/cm^3
Density glycerol/water solution, ρ_f^0	1.253 g/cm^3
Viscosity glycerol/water solution, μ_0	5.889 g/cm s
Maximum volume fraction, ϕ_{max}	0.64
Initial volume fraction, ϕ_0	0.20
Particle radius, a	0.0397 cm

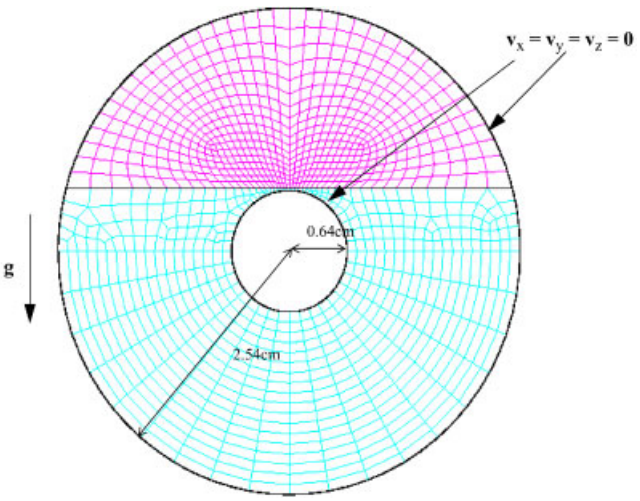

Figure 3. Finite element mesh and boundary conditions for particles settling in a Couette apparatus.

The mesh contains 4452 nodes, 1084 elements and 18 950 unknowns. The initial conditions are a constant volume fraction of 20%.

Figure 4 gives results from this mesh and from the NMR imaging for particle volume fraction. The modelling results also have velocity vectors superimposed on the concentration fields. The simulation results show an initially perfectly homogeneous particle distribution. After about 100 s, we see particles piling up below the rod and at the top of the cylinder. Complementary to this, clear zones of fluid form on top of the rod and at the bottom of the cylinder. What happens next is quite interesting. We see the clear fluid above the rod and the packed particles below the rod start shedding blobs of material, with the clear fluid sinking and the packed suspension rising. This leads to competing Rayleigh–Taylor instabilities, which create velocity fields that change direction first going upwards and then downwards, looking much like flapping wings when viewed dynamically. After 2600 s, the particles have all reached the top of the container, forming a packed zone with a flat interface and clear fluid below.

The results from the NMR imaging corroborate the simulations results. The suspension is initially well mixed and homogeneously distributed. Regions of maximum packing are shown in purple, white shows the pure fluid, and yellow shows the suspension. Over time, particles pile up

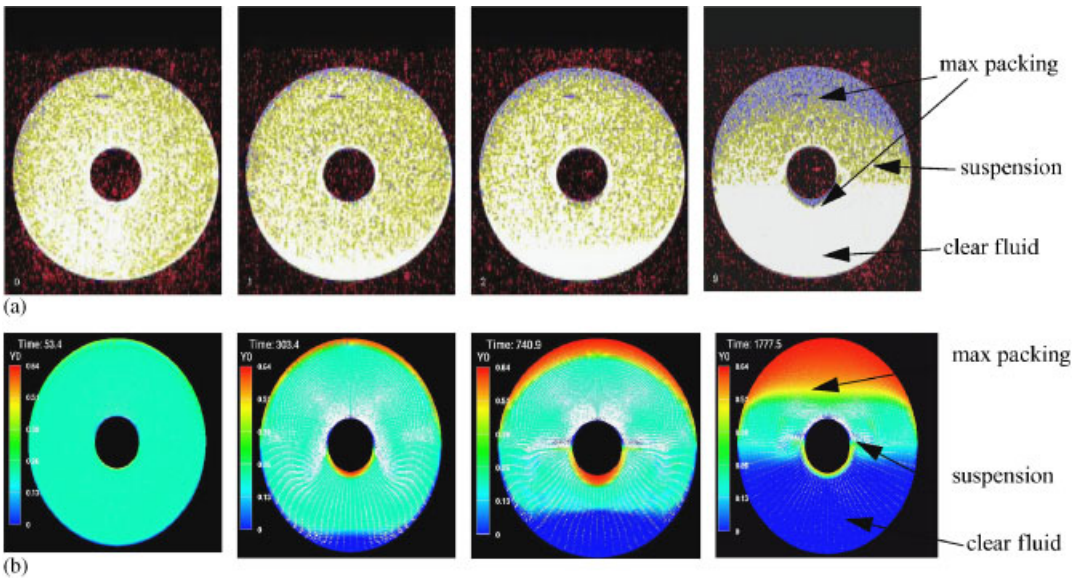

Figure 4. Results for 0.20 volume fraction PMMA particles suspended in a glycerol/water solution. Particles are floating in a horizontal Couette apparatus. Zones of maximum packing are seen at the top of the cylinder and beneath the inner cylinder: (a) NMR imaging $t = 68$, 204, 340, and 1156 s and (b) simulation $t = 53.4$, 303.4, 740.9, and 1777.5 s.

at the top of the container and below the rod, with clear fluid zones occurring above the rod and at the bottom of the Couette. We observe evidence of the instabilities seen in the simulation, since we can see low-concentration areas in the suspension similar to the blobs of pure fluid coming off the top of the rod. The final distribution of particles shows all particles settling at the top of the Couette with clear fluid below. Note that the timescales for the simulation and the experiment differ, but the simulations do capture the overall nonlinear phenomenology.

4.3. Quiescent particle flotation in a cylinder with a rectangular inclusion

4.3.1. Problem description. Particle flotation in a cylinder with a rectangular inclusion was investigated. The inclusion is actually another cylinder, but when seen in a 2-D axisymmetic slice, looks like a rectangle. The geometry and dimensions can be seen in Figure 5. The particles were glass microballoons (GMBs), which have a very low density. The suspending fluid used is 50-HB-500 Ucon lubricant, which has a density similar to water making the particles float. The initial volume fraction is almost 40%. Table III gives material properties for the suspension.

4.3.2. Simulation and comparison with experiment. The finite element mesh and boundary conditions can be seen in Figure 5. The mesh comprised 8777 nodes and 2100 elements, resulting in 24 421 unknowns. The boundary conditions are simply no slip at the solid surface. The initial condition is a constant particle fraction at 39.6% by volume.

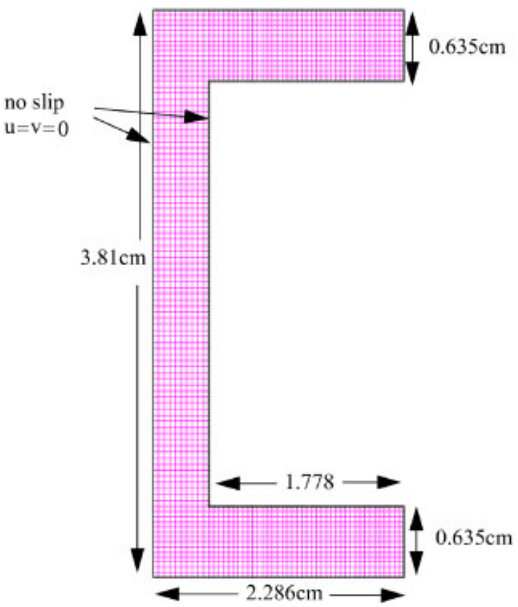

Figure 5. Finite element mesh and boundary conditions for particle flotation around a square inclusion.

Table III. Density, viscosity, and particle data for square inclusion experiment.

Quantity	Value
Density GMB, ρ_s^0	0.210 g/cm^3
Density 50-HB-400, ρ_f^0	1.041 g/cm^3
Viscosity 50-HB-400 solution, μ_0	1.5 g/cm s
Maximum volume fraction, ϕ_{max}	0.64
Initial volume fraction, ϕ_0	0.396
Particle radius, a	0.00295 cm

Figure 6 shows results for the particle volume fractions for the simulation and NMR imaging. For the simulation, the suspension starts out perfectly well mixed. After 810 s, we see particles getting trapped under the rectangular inclusion and a layer of maximum packing forming at the top of the cylinder. Clear zones have begun to form as well, as the bottom of the container and at the top of the rectangular inclusion. The concentrated suspension under the rectangle spawns streams of material into the narrow channel between the inclusion and the wall of the cylinder. Rayleigh–Taylor instabilities again occur as regions of low-density packed GMBs lie below higher-density suspension. This instability leads to remixing and chaotic flow profiles. Similarly, material streams off the top of the rectangle and moves down the narrow channel creating another zone of

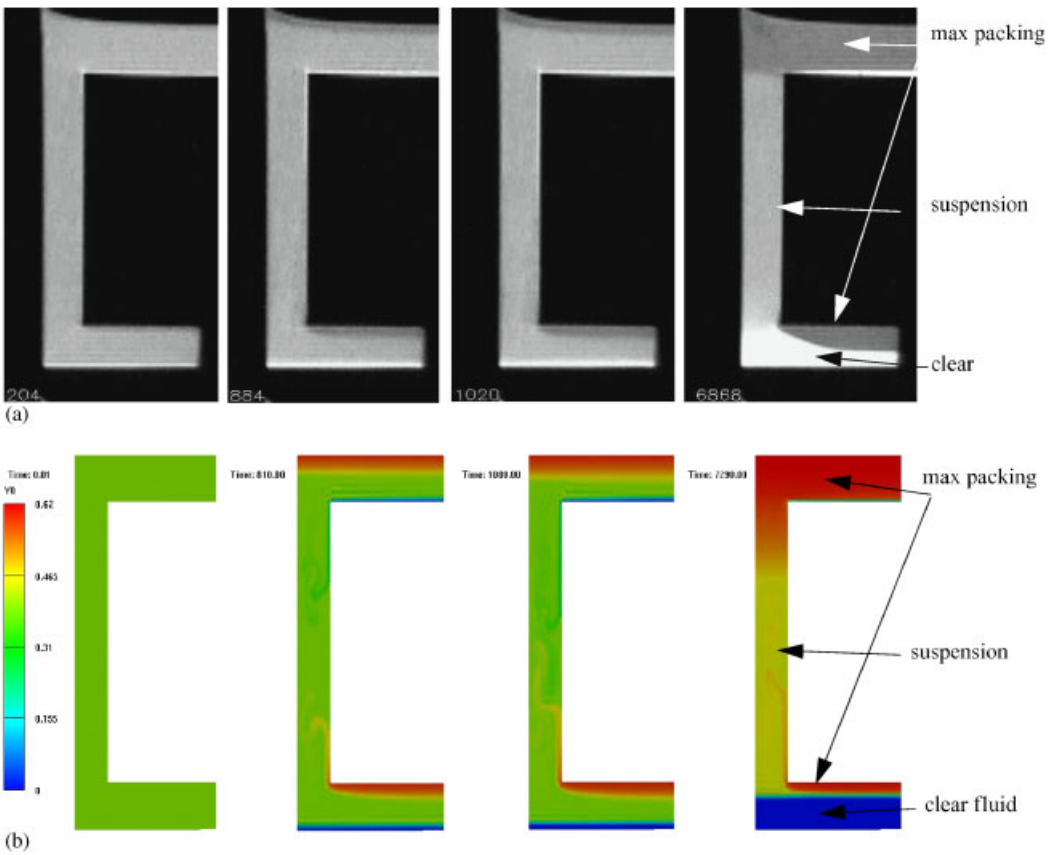

Figure 6. Particle flotation around a rectangular inclusion for 0.396 volume fraction of GMB in Ucon lubricant: volume fraction profiles as a function of time. Time stamp indicates elapsed time: (a) NMR imaging $t = 204$, 884, 1020, and 6858 s and (b) simulation $t = 0$, 810, 1080, and 7290 s.

instability where the heavier pure fluid is above the suspension. The same relative trends continue at 1080 s. At the final time plane shown, 7290 s, we can see that the clear zone above the rectangle has been replaced by suspension packed with particles to maximum packing. The instability below the inclusion remains and continues to spawn material that sinuously travels towards the top of the cylinder.

For the NMR imaging results, we see similar trends, though quantitative agreement is still elusive. The suspension starts off well mixed. After 884 s, we see clear layer forming above the inclusion and at the bottom of the container. Zones of maximum packing can be seen below the rectangle and at the top of the container. We can see some graininess that could be associated with streams of material remixing back into the suspension. This streaming phenomena is much easier to see when the images are viewed dynamically as a movie. Similar streaming trends continue at 1020 s. The final frame, 6868 s, shows that the top instability is gone and only the bottom instability remains. The shape of the packed zone under the inclusion is more curved in the experiment than the simulation.

Published in 2007 by John Wiley & Sons, Ltd. *Int. J. Numer. Meth. Fluids* 2007; **55**:723–735
DOI: 10.1002/fld

5. CONCLUSIONS

We have used NMR imaging and finite element modelling to help us understand the fluid mechanics involved in batch flotation and settling of suspensions in complex geometries. Particle settling in a cylinder with a contraction, particle flotation in a horizontal Couette, and particle flotation in a cylinder with a rectangular inclusion were investigated. It was determined that the complex geometries led to Rayleigh–Taylor instabilities, chaotic secondary flows, and remixing of segregated layers. Particle profiles were significantly different from what would be expected from monotonic batch settling experiments. This work underscores the usefulness of both NMR imaging and computational modelling for understanding the complex behaviour of suspensions of non-neutrally buoyant particles in geometries with inclusions and sharp corners and can help us design better manufacturing processes involving suspensions in non-monotonic geometries. For future work, we would like to investigate the effect of Reynolds and Grashof number on the instabilities. Preliminary experimental work has shown that the instabilities seen in the contracted cylinder at the parameters used here are not seen for heavier particles or more concentrated suspensions.

The instabilities seen in the NMR imaging often occur at shorter timescales from the simulation results though similar phenomenology for both simulation and experiment. For future work, we would like to achieve a more quantitative agreement between simulation and experiment.

ACKNOWLEDGEMENTS

Sandia is a multiprogram laboratory operated by Sandia Corporation, a Lockheed Martin Company for the United States Department of Energy's National Nuclear Security Administration under Contract DE-AC04-94AL85000. Partial support for this work was provided by the D.O.E. Office of Science Advanced Computing Research (ASCR) program in Applied Mathematical Sciences.

REFERENCES

1. Kynch GJ. A theory of sedimentation. *Transactions of Faraday Society* 1952; **48**:166–176.
2. Davis RH, Acrivos A. Sedimentation of noncolloidal particles at low Reynolds numbers. *Annual Review of Fluid Mechanics* 1985; **17**:91–118.
3. Fang Z, Phan-Thien N. Numerical Simulations of particle migration in concentrated suspensions by a finite volume method. *Journal of Non-Newtonian Fluid Mechanics* 1995; **58**:67–81.
4. Hofer M, Perktold K. Computer simulation of concentrated fluid-particle suspension flows in axisymmetric geometries. *Biorheology* 1997; **34**:261–279.
5. Subia SR, Ingber MS, Mondy LA, Altobelli SA, Graham AL. Modeling of concentrated suspensions using a continuum constitutive equation. *Journal of Fluid Mechanics* 1998; **373**:193–219.
6. Fang Z, Mammoli AA, Brady JF, Ingber MS, Mondy LA, Graham AL. Flow-aligned tensor models for suspension flow. *International Journal of Multiphase Flow* 2002; **28**:137–166.
7. Miller RM, Morris J. Development of a frame-invariant suspension flow model. *Advances in Fluid Mechanics* 2004; **37**:263–274; *Second International Conference on Computational Methods in Multiphase Flow*, *Multiphase Flow II*, Santa Fe, NM, United States, 3–5 November 2003.
8. Zhang K, Acrivos A. Viscous resuspension in fully developed laminar pipe flows. *International Journal of Multiphase Flow* 1994; **20**:579–591.
9. Schaflinger U, Acrivos A, Zhang K. Viscous resuspension of a sediment within laminar and stratified flow. *International Journal of Multiphase Flow* 1990; **16**:567–578.
10. Miskin I, Elliot E, Ingham DB, Hammond PS. Steady suspension flows into two-dimensional horizontal and inclined channels. *International Journal of Multiphase Flow* 1996; **22**:1223–1246.
11. Miskin I, Elliot E, Ingham DB, Hammond PS. The viscous resuspension of particles in an inclined rectangular fracture. *International Journal of Multiphase Flow* 1996; **22**:403–415.

12. Rao R, Mondy L, Sun A, Altobelli S. A numerical and experimental study of batch sedimentation and viscous resuspension. *International Journal for Numerical Methods in Fluids* 2002; **39**:465–482.
13. Phillips RJ, Armstrong RC, Brown RA, Graham AL, Abott JR. A constitutive equation for concentrated suspensions that accounts for shear-induced particle migration. *Physics of Fluids A* 1992; **4**:30–40.
14. Nott PR, Brady JF. Pressure-driven flow of suspensions: simulation and theory. *Journal of Fluid Mechanics* 1994; **275**:157–199.
15. Tirumkudulu M, Tripathi A, Acrivos A. Particle segregation in monodisperse shear suspension. *Physics of Fluids* 1999; **11**:507–509.
16. Timberlake BD, Morris JF. Concentrated band dynamics in free-surface suspension. *Physics of Fluids* 2002; **14**:1580–1589.
17. Timberlake BD, Morris JF. Particle migration and free-surface topology in inclined plane flow of a suspension. *Journal of Fluid Mechanics* 2005; **538**:309–341.
18. Tang H, Grivas W, Homentcovschi D, Geer J, Singler T. Stability considerations associated with the meniscoid particle band at advancing interfaces in Hele–Shaw suspension flows. *Physical Review Letters* 2000; **85**:2112–2115.
19. Jin B, Acrivos A. Theory of particle segregation in rimming flows of suspensions containing neutrally buoyant particles. *Physics of Fluids* 2004; **16**:641–651.
20. Carpen IC, Brady JF. Gravitational instabilities in suspension flow. *Journal of Fluid Mechanics* 2002; **472**:201–210.
21. Davis RH, Herbolzheimer E, Acrivos A. Wave formation and growth during sedimentation in narrow tilted channels. *Physics of Fluids* 1983; **26**:2055–2064.
22. Hernandez JA. Instabilities induce by concentration gradients in dusty gases. *Journal of Fluid Mechanics* 2001; **435**:247–260.
23. Leighton D, Acrivos A. Viscous resuspension. *Chemical Engineering Science* 1986; **6**:1377–1384.
24. Turney MA, Cheung MK, McCarthy MJ, Powell RL. Magnetic resonance imaging study of sedimenting suspension of noncolloidal spheres. *Physics of Fluids* 1995; **7**:904–911.
25. Lee S, Jang Y, Choi C, Lee T. Combined effect of sedimentation velocity fluctuation and self-sharpening on interface broadening. *Physics of Fluids A* 1992; **4**:2601–2606.
26. Altobelli SA, Mondy LA. Hindered flotation functions from nuclear magnetic resonance imaging. *Journal of Rheology* 2002; **46**:1341–1352.
27. Watkins JC, Fukushima E. The highpass birdcage coil for NMR. *Review of Scientific Instrumentation* 1988; **59**:926–929.
28. Callaghan PT. *Principles of Nuclear Magnetic Resonance Microscopy*. Oxford University Press: New York, 1991.
29. Krieger IM. Rheology of monodisperse lattices. *Advances in Colloid Interface Science* 1972; **3**:111–136.
30. Tetlow N, Graham AL, Ingber MS, Subia SR, Mondy LA, Altobelli SA. Particle migration in a Couette apparatus: experimental and modeling. *Journal of Rheology* 1998; **42**:307–327.
31. Donea J. A Taylor–Galerkin method for convective transport problems. *International Journal for Numerical Methods in Engineering* 1984; **20**:101–119.